

1 Article

2 The multilevel structure of sulfonated 3 syndiotactic-polystyrene model polyelectrolyte 4 membranes resolved by extended Q-range contrast 5 variation SANS.

6 Maria-Maddalena Schiavone ¹, Hiroki Iwase ², Shin-ichi Takata ³, and Aurel Radulescu ^{1,*}7 ¹ Jülich Centre for Neutron Science (JCNS) at Heinz Maier-Leibnitz Zentrum (MLZ), Forschungszentrum
8 Jülich GmbH, 85747 Garching, Germany9 ² Neutron Science and Technology Center, Comprehensive Research Organization for Science and Society
10 (CROSS), 162-1 Shirakata, Tokai, Ibaraki 319-1106, Japan11 ³ Materials and Life Science Division, Japan Proton Accelerator Research Complex (JPARC), Tokai, Ibaraki
12 319-1195, Japan

13 * Correspondence: a.radulescu@fz-juelich.de; Tel.: +49-89-289-10712 (A.R.)

14

15 **Abstract:** Membranes based on sulfonated syndiotactic polystyrene (s-sPS) were thoroughly
16 characterized by contrast variation SANS over a wide Q-range in dry and hydrated states.
17 Following special sulfonation and treatment procedures s-sPS may become an attractive material
18 for fuel cells and energy storage applications. The film samples were prepared by solid-state
19 sulfonation that allowed a uniform sulfonation of only the amorphous phase while preserving the
20 crystallinity of the membrane. The samples were loaded with different guest molecules in either
21 the amorphous (fullerenes) or the crystalline (toluene) regions, in order to vary the neutron contrast
22 or to reproduce the conditions enabling an increased resistance of the membranes to chemical
23 decomposition. The use of uni-axially deformed film samples and contrast variation with different
24 H₂O/D₂O mixtures allowed for the identification and characterization of different structural levels
25 with sizes between nm and μ m, which form and evolve in the membrane morphology in dry and
26 hydrated states and produce scattering features on different detection sectors and at different
27 detection distances after the sample, depending on their size and orientation.

28 **Keywords:** proton exchange membranes; semi-crystalline polymers; small-angle neutron scattering

29 1. Introduction

30 Owing their high conversion efficiency, high power density, low weight and volume, fast
31 startup time, low operating temperature (below 100°C) and clean exhaust, the polymer electrolyte
32 membrane (PEM) fuel cells (PEMFC) are considered an attractive energy conversion technology for
33 transportation applications, as demonstrated by the prototyped fuel cell vehicles and announced
34 near future production plans by almost all major car manufacturers [1,2]. With potential to become
35 an alternative to the currently used fossil fuel technologies in light-duty transportation and to reduce
36 thus the dependence on conventional fuels and the CO₂ emissions, PEMFCs show not only
37 economical, but also environmental benefits.

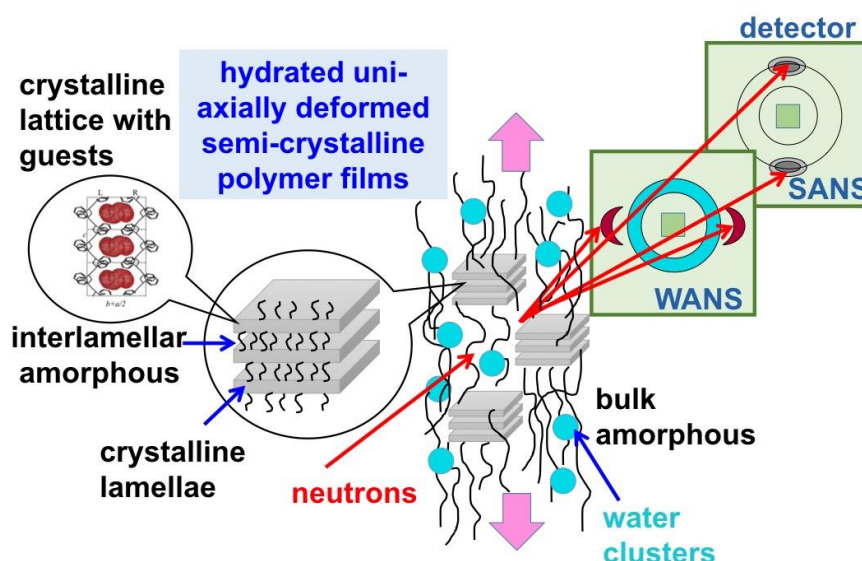
38 In a simplistic picture of the working principle of a PEMFC, the PEM separates the anode from
39 the cathode and conducts at very high rates the protons emerging from the catalyst facilitated
40 hydrogen oxidation in the anode chamber [3]. However, the transport phenomenon in the PEM is a
41 complex process because, on one hand, besides protons that are the only ones to be transferred
42 through the membrane, other species are produced at the anode too, and, on the other hand, the
43 leaking of fuel (hydrogen) and oxidant (air) from the anode chamber to the counterpart must be

44 prevented [4]. Moreover, a very efficient PEMFC requires the membrane to function in hydrated
45 state, which usually lowers the mechanical strength. Therefore, great efforts have been spent in the
46 last years to develop and characterize materials that are approaching the properties of an ideal
47 "separator" [5] and to understand and optimize the water management in different components of
48 the PEMFC [6-8]. PEM materials should be characterized by a nanoscale phase separation into
49 hydrophilic domains and hydrophobic regions, a combination that enables a high conductivity and
50 provides a good chemical and mechanical stability, thus membrane durability. Perfluorosulfonated
51 ionomers (PFSI) present high performances and stability in PEMFC operational conditions. Among
52 them, the Nafion (Du PontTM) is the most well known material and was established as benchmark for
53 such applications [9]. However, despite their excellent properties, the PSFI materials present several
54 drawbacks such as the high cost, lack of safety during manufacturing and use, requirement of
55 supporting equipment and temperature related limitations [10]. Thus the PSFI membranes seem not
56 to be still the ideal choice for the commercialization of PEMFC technology. Alternative low-cost
57 materials that should present similar conductive and chemo-mechanical properties as the PFSI
58 membranes are continuously searched for. Different crystalline-amorphous polymer architectures
59 and the interrelation of their properties with the microphase separation structures, such as
60 crystalline domains, the formation of conducting regions, and the distribution of ionic groups and
61 water in the conducting regions were extensively studied in last years [11-15]. Given the recent
62 developments, which enable a controlled sulfonation of only the amorphous phase, preserving thus
63 the crystallinity of the material [16], and an improved resistance to oxidation decomposition when
64 fullerenes are added [17], the sulfonated syndiotactic polystyrene (s-sPS) in its β -form may become a
65 good candidate for some PEMFC applications, as it presents a high proton conductivity, comparable
66 to Nafion [18], high chemical and thermo-mechanical stability and a low cost [19]. The preparation of
67 s-sPS membrane should start from the δ -form (clathrate with guest molecules), which enables a
68 homogeneous sulfonation of the amorphous regions only and can be subsequently transformed into
69 the thermodynamically stable β -form by chemical/annealing treatment [18, 20]. On the other hand,
70 SPS based membranes may also found application in the energy storage field, for increasing the
71 safety of high temperature operating Li-ion batteries, for example [21].

72 The nano-morphology of PEM materials, and together with this the elucidation of water
73 domains and conductive paths at microscopic level, are a highly debated topic. Even in the case of
74 Nafion several microstructural models are still under consideration [22]. In a previous work [23] we
75 reported a detailed microstructural characterization of highly sulfonated membranes (above 50%
76 sulfonation degree) based on an s-sPS δ -clathrate co-crystalline form [24, 25]. The microstructural
77 characterization was carried out by small-angle neutron scattering (SANS) during the complex
78 preparation procedure of the membranes, from the production of the sPS film samples in α -form
79 followed by clathration with toluene guest molecules (to yield the δ -form [26]), sulfonation and
80 *in-situ* hydration under controlled relative humidity (RH) by using a humidity chamber (Anton
81 Paar). The use of uniaxially deformed sPS films enabled the assignment of the scattering signals
82 observed on different sectors of the SANS detector to specific morphologies that formed and
83 evolved in the sample during the clathration, sulfonation and hydration/dehydration processes.
84 Besides the structural characterization of the crystalline lamellar stacks and the water cluster
85 morphologies evolving in the amorphous regions with increasing the RH, information on the
86 mechanical strength and stability of the membranes due to preservation of crystallinity could be
87 assumed from the interpretation of the SANS data and confirmed at a later time in subsequent
88 experiments by wide-angle X-ray diffraction (WAXD).

89 In this paper we report a structural investigation by contrast variation SANS on uniaxially
90 deformed s-sPS films containing the crystalline δ -form that were prepared with different degrees of
91 sulfonation. The films were loaded with fullerenes, in order to reproduce the conditions proposed
92 for such materials to reach the optimal chemical stability in PEMFC environment. The SANS
93 experiments were carried out over a wide wave-vector transfer Q-range, between 0.001 and 2 \AA^{-1} ,
94 which enabled the observation of scattering features from morphologies and structures formed at
95 very different length scales in the membranes, such as the 010 crystalline peak of the crystalline

96 lattice characteristic of the lamellae in the crystalline domains, the ionomic peak representing the
 97 structural correlation length for the ionic hydrophilic domains in the amorphous regions, the
 98 inter-lamellar peak representing the correlation length between the crystalline lamellae, the form
 99 factor of the water domains and the large scale fractal of the membranes. Thus, a very extended
 100 length scale, from a few Å to nm, could be explored in this investigation. Due to the uni-axially
 101 deformation of the films, some of the scattering details from these morphologies appear distributed
 102 on specific detector sectors, like the features characteristic of crystalline domains: the 010 crystalline
 103 peaks appear on equatorial sectors while the inter-lamellar peaks in the meridian sectors direction.
 104 Other morphologies yield scattering that is isotropically distributed over the detection area, like the
 105 features from the amorphous regions, thus the ionomer peak and the water domains form factor. A
 106 schematic view of the experimental geometry approach used in this study and of the novelty we
 107 have implemented compared to our previous approach [23] is shown in Figure 1.
 108



109
 110
 111
 112
 113
 114

Figure 1. Schematic view of the experimental approach used in this study: the uni-axially polymer film deformation is indicated by the pink arrows while the morphologies occurring at different length scales, which are shown in the left side of the scheme, yield on the two-dimensional SANS detector scattering features that appear at different scattering angles, either in the wide-angle (WANS) or small-angle (SANS) regime, as isotropic or localized details.

115
 116
 117
 118
 119
 120
 121
 122

In order to minimize the SANS incoherent background, deuterated sPS films have been used in the study. Contrast variation method was involved to vary the scattering length density (SLD) of different film components in a controlled way, i.e. by using either deuterated or protonated species for the guest molecules in the crystalline regions, or different $\text{H}_2\text{O}/\text{D}_2\text{O}$ mixtures for the hydration of the membranes. Thus, the formation and evolution of all these morphologies during hydration process could be fully understood following the model interpretation of the scattering curves, which were averaged over the meridian and equatorial sectors for each contrast condition.

123 2. Materials and Methods

124 2.1. Materials

125 The preparation and subsequent treatment – clathration, sulfonation, guest-exchange in the
 126 crystalline region – of uni-axially deformed deuterated syndiotactic polystyrene films were done
 127 following a procedure that is extensively described in [23]. Films with variable degree of sulfonation
 128 were produced via so-called solid-state sulfonation procedure that allowed a uniform sulfonation of
 129 the phenyl rings of the amorphous phase and preserved the crystalline δ -form [16]. The thickness of

130 the films was about 100 μm . To vary the neutron scattering contrast, either deuterated or protonated
131 toluene were loaded as guest in the clathrate form, either before or after sulfonation, by dipping the
132 films for 1 day in solvent, followed by drying at 40 $^{\circ}\text{C}$ under vacuum for a couple of hours.
133 Fullerenes C60 or C70 were uploaded in some of the s-sPS membranes by dipping the samples for
134 more than three weeks in saturated solution of fullerenes and protonated toluene. Two selected
135 films of different composition were subjected during the SANS experiments to *in-situ* controlled
136 hydration under vapors of different $\text{H}_2\text{O}/\text{D}_2\text{O}$ mixtures, by using a humidity chamber [23]. All
137 reagents were purchased from Sigma-Aldrich and used as received. The D_2O was obtained from
138 Cambridge Isotope Laboratories (purity D 99.8%).
139

140 2.2. Methods

141
142 The degree of sulfonation was checked at the neutron prompt-gamma activation analysis
143 (PGAA) instrument of Technical University München (TUM) installed at the Heinz Maier-Leibnitz
144 Zentrum (MLZ), Garching, Germany. Description of the experimental method and data
145 interpretation can be found in [23].

146 Qualitative and quantitative analysis of the sulfonation, the loading with fullerenes and the
147 crystallinity of the s-sPS films was checked by FTIR using a PerkinElmer (Spectrum Two)
148 spectrometer equipped with a TGS detector. The scanned wavenumber range was 4000 - 400 cm^{-1} .

149 WAXD analysis of sulfonated films with and without fullerenes added was done prior to the
150 SANS experiments in the range of 2θ between 5 $^{\circ}$ and 35 $^{\circ}$ by means of an X-ray powder
151 diffractometer Brucker 2nd Gen-D2 Phaser (Cu-source) of Jülich Centre for Neutron Science (JCNS) at
152 MLZ.

153 UV-Vis analysis of the same films was carried out with a Cary 100 SCAN UV-Vis Varian
154 spectrometer of JCNS at MLZ with the films placed in a specific holder with quartz windows. The
155 spectra were collected in the range 200-800 nm at a resolution of 100 nm/min.

156 Preliminary SANS measurements were carried out at the KWS-2 high intensity / extended-Q
157 range pinhole SANS diffractometer of JCNS at MLZ [27]. A Q-range between 0.02 and 0.7 \AA^{-1} was
158 covered in this preparatory experiments by using two sample-to-detector distances, $L_D=1.5$ m and 4
159 m and a neutron wavelength $\lambda=4.5$ \AA . The film samples were placed in beam by means of
160 sandwich-type cells with Quarz windows.
161

162 **Table 1.** The calculated SLD for different components of the s-sPS films.

Compound	SLD, $\times 10^{10} \text{ cm}^{-2}$
sPS (crystalline)	6.47
sPS (amorphous)	6.00
s-sPS (amorphous)	6.34
-SO ₃ H	1.32 (1.1 [28])
D ₂ O	6.38
H ₂ O	-0.56
d-Tol	5.66
h-Tol	0.94
C60	5.50
C70	5.67

163

164 Extended Q-range SANS experiments have been performed at the time-of-flight (TOF) SANS
165 diffractometer TAIKAN, at the Material and Life Science Experimental Facility (MLF) of the Japan
166 Proton Accelerator Research Facility (J-PARC), Tokai, Japan [29]. A Q-range between 0.008 and 2 \AA^{-1}
167 was covered by using a broad neutron wavelength range $\lambda = 0.7$ to 7.8 \AA and the simultaneous use of

168 only the small-angle and middle-angle detector banks (due to restrictions imposed by the sample
 169 environment). Involving the additional use of the wide-angle and back-scattering detector banks,
 170 which are available at this instrument too, a $Q_{\max}=20 \text{ \AA}^{-1}$ could be otherwise reached in a single
 171 measurement for a sample geometry that would allow detection of the scattered neutrons in a wide
 172 angular range. At TAIKAN the film samples were exposed to *in-situ* controlled hydration within the
 173 range $\text{RH} = 50\%$ to 80% by the mean of an Anton-Paar humidity chamber [23]. Contrast variation
 174 SANS measurements were carried out by exposing the sample to mixed $\text{H}_2\text{O}/\text{D}_2\text{O}$ vapors for
 175 different ratios of the two components at $\text{RH} = 80\%$.

176 At both SANS instruments the raw data was treated by standard corrections and reduction
 177 procedure [27, 29] and then calibrated in absolute units by using a Plexiglas (at KWS-2) or a
 178 glassy-carbon (at TAIKAN) secondary standard. The corrected and calibrated 2D data were
 179 integrated into one-dimensional intensity over equatorial or meridian sectors of a 20° width. The
 180 SLD for different compounds in the s-sPS film morphology are listed in Table 1, as it was calculated
 181 or taken from literature.
 182

183 *2.3. Data analysis*

184
 185 Supposing we have N identical particles of volume V_p , which are located at random positions
 186 and random orientations in the sample, then $NV_p=\phi V_{\text{sample}}$, where ϕ is the volume fraction of the
 187 scattering particles in the sample. The contribution to the small-angle scattering intensity from these
 188 particles that are decorated with a constant contrast factor $\Delta\rho$ is

189
$$I(Q) = \phi \Delta\rho^2 V_p P(Q) S(Q) + \text{Bckgd} \quad (1)$$

190 where $P(Q)$ represents the particle form factor, which relates to the intra-particle correlations,
 191 and $S(Q)$ the structure factor, which denotes the inter-particle correlation effects. The contrast
 192 $\Delta\rho=\rho_p-\rho_{\text{env}}$ is the difference between the SLD of the scattering particles ρ_p and their environment ρ_{env} ,
 193 where the environment can be a solvent, a film, or a metallic matrix. Usually, the factor $(\phi \Delta\rho^2 V_p)$ is
 194 called the “forward scattering” I_0 from the ensemble of scattering particles. The term Bckgd
 195 represents a constant background, which arises mostly from the incoherent scattering contribution
 196 and can be observed as a constant level at high Q .

197 In the current study we used the combination of the form factor and the structure factor to
 198 describe the scattering from the water domains in the amorphous phase of the s-sPS films and the
 199 lamellar stacks in the crystalline regions. For the water clusters the spherical form factor

200
$$P_{\text{sph}}(Q) = \left[3 \frac{\sin(QR) - QR \cos(QR)}{(QR)^2} \right]^2 \quad (2)$$

201 was combined with the hard-sphere structure factor [29]

202
$$S(Q, R_{\text{HS}}) = [1 + 24 \eta_{\text{HS}} G(R_{\text{HS}}Q)/(R_{\text{HS}}Q)]^{-1} \quad (3)$$

203 where R is the radius of the spherical cluster, R_{HS} the “hard sphere” radius of the interaction
 204 potential and η_{HS} the volume fraction of hard spheres. The function $G(R_{\text{HS}}Q)$ has a complicated
 205 analytical dependence on η_{HS} [30]. The lamellar stacks consisting of oriented crystalline lamellae that
 206 alternate with amorphous inter-lamellar regions was described by the two-dimensional
 207 crystalline-amorphous form factor [31], where crystalline lamellae have amorphous layers attached
 208 on both faces:

209
$$P_{\text{lam}}(Q) = (\Delta\rho_{\text{cr}} P_{\text{cr}}(Q) + \Delta\rho_{\text{am}} P_{\text{am}}(Q))^2 \frac{D(QR_{\text{I}}/2)}{(QR_{\text{I}}/2)} (\pi R_{\text{I}}^2)^2 \quad (4)$$

210 in combination with the paracrystalline structure factor

211
$$S_{\text{para}}(Q) = \frac{\sinh(Q^2 \sigma_D^2/4)}{\cosh(Q^2 \sigma_D^2/4) - \cos(QL_D)} \quad (5)$$

212 where L_D is the inter-lamellar distance (periodicity), σ_D its dispersion and R_i the lateral size of
 213 the lamellae. Because we are dealing here with a ternary system consisting of the crystalline
 214 lamellae, the inter-lamellar amorphous region and the surrounding bulk amorphous region, the
 215 contrast factor from Eq. 1 was included in the form factor definition in Eq. 4, with the aim to express
 216 the difference in SLD between these three components. The Dawson function $D(u)$ exhibits the
 217 following asymptotic behavior: for $u \rightarrow \infty$, $2D(u) \rightarrow 1/u^2$ and for $u \rightarrow 0$, $D(u)/u \rightarrow 1$. The partial form
 218 factor of the crystalline lamellae $P_{cr}(Q)$ is given by

$$219 \quad P_{cr}(Q) = \left[\frac{\sin(\frac{Qd}{2})}{\frac{Qd}{2}} \right]^2 \quad (6)$$

220 with d – the lamellar thickness, while the partial form factor of the inter-lamellar amorphous
 221 layers $P_{am}(Q)$ has a complicated analytical definition [31] that depends on both the lamellar thickness
 222 d and the thickness of the inter-lamellar layer L_b . Hence, $L_D = d + L_b$. The SLD for three distinct regions
 223 of the modeled morphology were explicitly considered in the fitting procedure: ρ_{lam} – the SLD of the
 224 crystalline sPS, $\rho_{inter-lam}$ – the SLD of the sulfonated inter-lamellar amorphous region, and ρ_{bulk} – the
 225 SLD of the sulfonated bulk amorphous region. Thus, the contrast factors in Eq. 4 are $\Delta\rho_{cr} = \rho_{lam} - \rho_{bulk}$
 226 and $\Delta\rho_{am} = \rho_{inter-lam} - \rho_{bulk}$. These three regions are affected in a different way by hydration. The bulk
 227 and inter-lamellar amorphous regions are hydrated, so they swell upon water uploading, as
 228 reported before [23]. Therefore their SLD is changed according to

$$229 \quad \rho_{bulk, inter-lam} = (\phi_{pol}\rho_{s-sPS} + \phi_{water}\rho_{water}) \quad (7)$$

230 with ρ_{s-sPS} and ρ_{water} – the SLD for the sulfonated polymer and the H_2O , D_2O or H_2O/D_2O
 231 mixtures, as defined in Table 1, and ϕ_{pol} and ϕ_{water} – the volume fractions of polymer and hydrated
 232 water in the swollen amorphous regions. Disregarding the free volume in the amorphous polymer,
 233 which typically is very small [32], we can roughly assume that $\phi_{water} = 1 - \phi_{pol}$ in these regions.

234 The global water fraction in the amorphous phase can be determined from the interpretation of
 235 the “forward scattering” from the water domains. However, there is an unknown partition of water
 236 between the bulk and inter-lamellar amorphous regions. Moreover, due to the loading with guest
 237 molecules, either protonated toluene or fullerenes, the SLD of the lamellar region is lower than that
 238 of the crystalline sPS (Table 1). Therefore, in the fitting procedure of the experimental data from the
 239 lamellar stacks (Eq. 1, 4-6), the SLD parameters ρ_{lam} and $\rho_{inter-lam}$ were considered free parameters.
 240 The ρ_{bulk} in this procedure was considered that of the amorphous sPS (Table 1). This is a reasonable
 241 assumption if we consider that the sulfonated segments of the sPS chains in the bulk region are
 242 contained in the water domains, thus not affecting the SLD of the amorphous segments in the
 243 vicinity of the lamellar stacks. The obtained value for $\rho_{inter-lam}$ was further used for rationalization on
 244 the polymer volume fraction and water content in the inter-lamellar amorphous regions (Eq. 7). On
 245 the other hand, the crystalline lamellae are not hydrated therefore the ρ_{lam} delivered by the fitting
 246 procedure was used for the estimation of the amount of guest molecule included in the crystalline
 247 region, in a similar way as shown in Eq. 7, with the guest molecule instead of water. According to
 248 [25], the amount of guest molecules included in the crystalline region may vary up to about 9% in
 249 case of δ -clathrate form. Therefore, the SLD of the crystalline region in our films may decrease from
 250 the value reported in Table 1 for the crystalline sPS up to $\rho_{lam}=5.9 \times 10^{10} \text{ cm}^{-2}$, taking into account the
 251 contribution of the protonated toluene to the overall SLD of the crystalline region.

252 3. Results and Discussion

253 3.1. Composition and crystallinity characterization.

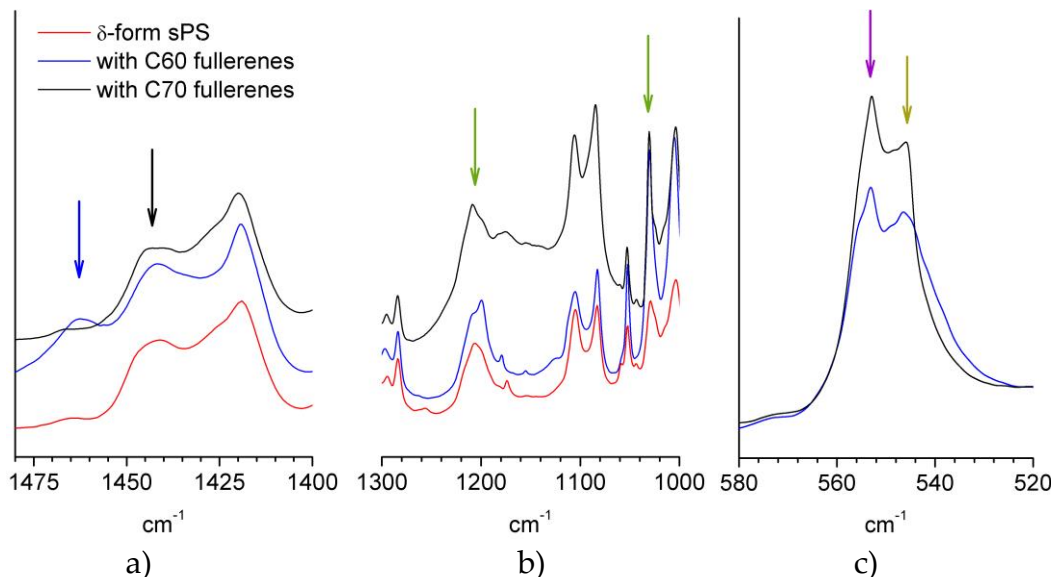
254

255 From the quantitative point of view, PGAA delivered the S/C ratio of 0.065 and 0.155 for the
 256 two uni-axially deformed sPS films studied in this work. Following the method reported in [33],
 257 which was used also in our previous study [23], sulfonation degrees of S=19.5 % and 46.3 % (molar

258 fraction of sulfonated monomer units) were determined for the samples which were later subjects of
 259 doping with C60 and C70 fullerenes, respectively.

260 The FTIR spectra of these films doped with C60 (blue curves) or C70 (black curves) fullerenes
 261 are shown in Figure 2 in parallel to that from a δ -form sPS film (red curve). The regions of fullerenes
 262 (Figure 2a) and of symmetric and asymmetric stretching of SO_3^- group (Figure 2b) were selected
 263 from the whole FTIR spectra collected from these samples. The bands corresponding to the sulfonic
 264 group were observed at around 1240 and 1040 cm^{-1} , which is in good agreement with early reports
 265 on sulfonated copolymers [34, 35]. Due to the multitude of characteristic bands of sPS, only some of
 266 the characteristic bands to C60 and C70 may be observed in the region 1440-1470 cm^{-1} . Experimental
 267 FTIR characterization of fullerenes in bulk or functionalized polymers can be found in [36] for C60 or
 268 [37] for C70, while theoretical calculations were done in [38]. From the evaluation of the bands that
 269 are characteristic to crystalline and amorphous sPS, a satisfactory estimation of the amount of
 270 polymer in the ordered TTGG sequences in the co-crystalline film samples can be obtained following
 271 the procedure described in [39]. Thus, a rough idea about the crystallinity of the sample can be
 272 obtained. Information about the FTIR spectra from deuterated sPS either in film or solution/gel
 273 samples is very scarce in literature. Therefore, for this exercise we considered the bands in the range
 274 500-600 cm^{-1} , a range that was never discussed before in the case of the deuterated sPS system and,
 275 which, according to our investigations on crystallization from solution (results to be published
 276 soon), contains information about either the helical or amorphous polymer chain conformation.
 277 Figure 2c shows two peaks for each sample, which can be assigned to the sPS in crystalline (556 cm^{-1})
 278 or amorphous (545 cm^{-1}) phases. From the interpretation of the areas of the peaks, the fraction of
 279 conformationally ordered polymer is about 35% and 22% for the films with higher sulfonation
 280 degree (loaded with C70) and lower sulfonation degree (loaded with C60), respectively.

281



282

283

284 **Figure 2.** FTIR spectra from different sPS films: δ -form (red line), sulfonated and loaded with C60
 285 fullerenes (blue line); sulfonated and loaded with C70 fullerenes (black line). The regions with
 286 fullerenes bands (C60 – blue arrow; C70 – black arrow) and sulfonic ionic group group bands (green
 287 arrows) are shown in the panels a) and b), respectively. Panel c) shows the bands characteristic of
 288 sPS: the arrows indicate the peaks that were considered to correspond to chain conformations in
 289 crystalline (purple) and amorphous (dark yellow) phases.

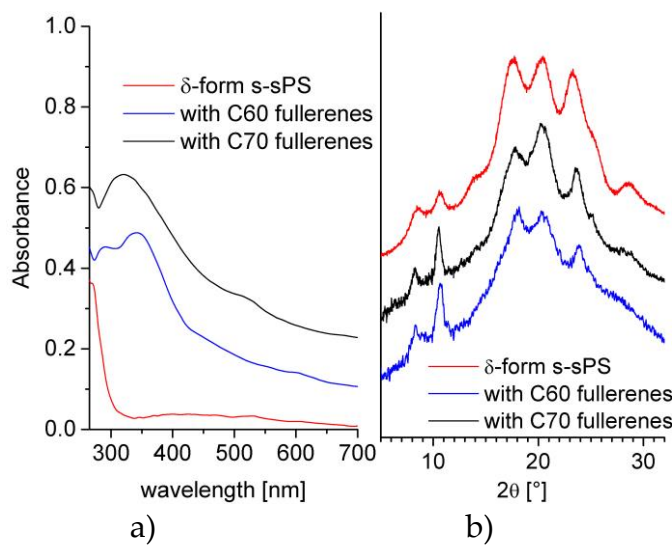
290

291 In Figure 3a, UV-Vis absorption spectra of the three samples are shown in parallel. Unlike the
 292 case of the δ -form s-sPS film, two spectral features are observed for the samples containing
 293 fullerenes: at around 330 nm (peak) and 400 nm (shoulder like) for the film doped with C60, and
 294 around 320 and 500 nm for the sample with C70, as a prominent and a weak peak, respectively.

295 These observations are also in good agreement with reported results in [36, 40, 41]. The PGAA, FTIR
296 and UV-Vis results confirmed the successful sulfonation and loading of the sPS membranes with
297 either C60 or C70 fullerenes.

298 WAXD spectra from the s-sPS films containing fullerenes are presented in the Figure 3b in
299 parallel with the pattern from the s-sPS film with only protonated toluene loaded in the crystalline
300 regions (clathrates). The pair of peaks at around 8° and 10° in 2θ is indicative for the formation of the
301 crystalline δ-form of the clathrates [24, 42]. The presence of these peaks in the patterns collected on
302 the samples loaded with fullerenes indicates that the sPS crystalline habit is preserved in these
303 samples too. Their slight enhancement when C60 or C70 fullerenes were added may relate to
304 anchoring of the fullerenes to the sPS chains, as it was discussed in [42]. Because the detailed
305 analysis of WAXD spectra and of fullerenes behavior in s-sPS films is beyond the goal of this work,
306 we limit ourselves here to a qualitative conclusion. Based on the characterization methods applied
307 prior to SANS on our samples, we can confirm the presence of the crystalline δ-form in all films and
308 the loading of samples with fullerenes, and we may only suppose that in some of the cavities
309 between the sPS helices in the crystalline region the protonated toluene initial guest was replaced by
310 the fullerenes.

311

312
313

314 **Figure 3.** UV-Vis (a) and WAXS (b) spectra from different sPS films. The lines indicate sulfonated
315 film with crystalline δ-form (red line), sulfonated (with crystalline δ-form) and loaded with C60
316 fullerenes (blue line); sulfonated (with crystalline δ-form) and loaded with C70 fullerenes (black
317 line).

318

319 3.2. SANS on dry films

320

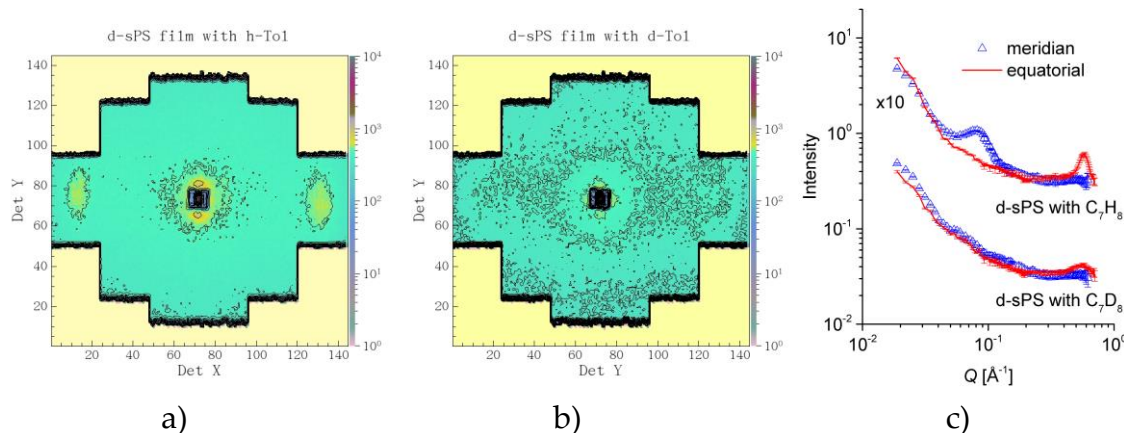
321 The main objective of this work is the microstructural characterization of the s-sPS membranes
322 under hydration and the understanding of the formation and evolution of morphologies at nano-
323 and meso-scale. In our previous study [23] we discussed the indirect observation on the preservation
324 of crystallinity in such systems during the chemical treatment and hydration procedures. A direct
325 observation of this effect together with a detailed microstructural characterization of the membranes
326 over a wide length scale can be achieved by using the contrast variation SANS over a wide Q-range.
327 This enables the collection of the scattering features from the crystalline ordering in the range of
328 nanometers up to the micrometer size large-scale domains in one experiment. For this purpose, the
329 novel approach that involves careful SANS measurements at high angle was checked first at the
330 KWS-2 SANS instrument in combination with the contrast variation method on two δ-clathrate sPS

331 films with toluene as guest in the cavities between the polymer helices: one film was investigated as
 332 produced, while the other one after subsequent sulfonation and loading with C₇₀ fullerenes.

333 In Figure 4 the scattering patterns from the uni-axially deformed sPS film containing clathrate
 334 co-crystalline δ -form with either protonated toluene or deuterated toluene are shown in
 335 two-dimensional (Figures 4a and b) and one-dimensional (Figure 4c) presentations, respectively,
 336 following the averaging over the meridian and equatorial sectors. In Figure 4a two strong maxima
 337 can be observed in equatorial sectors at high angles while two local maxima can be distinguished at
 338 low scattering angles in meridian direction, above and below the beam-stop, which is visible in the
 339 middle of the detector. These are the 010 reflections appearing on the equator and the inter-lamellar
 340 reflections on the meridian, respectively, as depicted in the sketch presented in Figure 1. In Figure 4b
 341 these features are either barely observable (the 010 reflections) or vanished (the inter-lamellar
 342 reflections). These features are also depicted by the one-dimensional patterns in Figure 4c. The 010
 343 reflections are yielded by the correlation between polymer sheets that sandwich in between the
 344 guest molecules. The SLD of deuterated crystalline sPS is $\rho=6.47 \times 10^{10} \text{ cm}^{-2}$, while that of the toluene
 345 is $\rho=0.94 \times 10^{10} \text{ cm}^{-2}$ and $\rho=5.66 \times 10^{10} \text{ cm}^{-2}$ for the protonated and deuterated species, respectively.
 346 Thus, protonated toluene molecules hosted between deuterated sPS helices is providing a high
 347 neutron contrast, which evidences at best the correlation between 010 planes (see Figure 1, the
 348 crystalline lattice details). In case of using deuterated toluene guests, the neutron contrast is much
 349 lower and the peaks on the equator become less obvious in the scattering pattern.

350 On the other hand, the inter-lamellar correlation peaks appear due to the difference in SLD
 351 between the amorphous and crystalline regions of the sPS co-crystals with guest molecules. The SLD
 352 of the amorphous sPS is $\rho=6 \times 10^{10} \text{ cm}^{-2}$. Loading the crystalline regions with protonated toluene will
 353 provide those regions with a lower SLD than the inter-lamellar amorphous regions, which will
 354 evidence the inter-lamellar correlations. Contrariwise, by using deuterated toluene the difference in
 355 SLD between the crystalline lamellae and inter-lamellar amorphous regions will become much
 356 smaller than in the case of using protonated toluene, which will have as consequence the vanishing
 357 of the inter-lamellar peaks on the meridian direction in the scattering patterns. Detailed SANS
 358 studies on the exchange of small guest molecules in sPS co-crystals are reported in [26, 43].

359
 360



361
 362

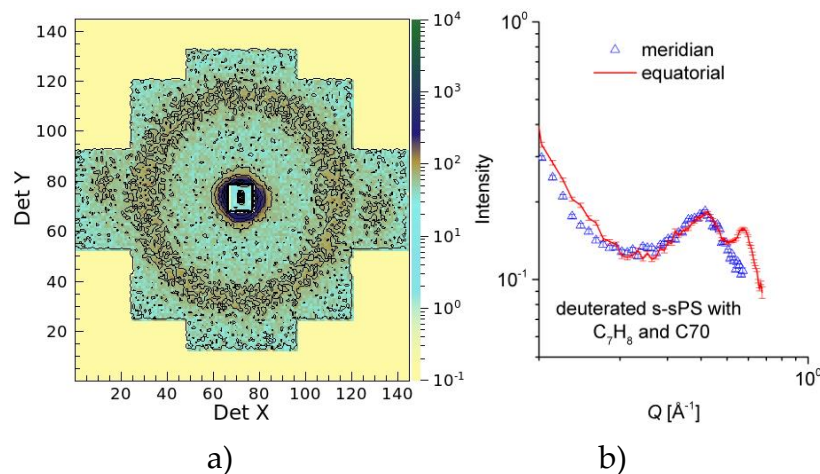
363 **Figure 4.** Two-dimensional SANS patterns from a deuterated sPS film clathrated with protonated
 364 toluene (a) or deuterated toluene (b), respectively, and the one-dimensional scattering profiles from
 365 the same samples averaged over the equatorial (line) or meridian (symbol) directions, respectively
 366 (c). The panels a) and b) show data collected at $L_D=2\text{m}$ while the experimental curves in panel c) were
 367 obtained by merging data collected at $L_D=2\text{m}$ and 4m .

368
 369
 370
 371

This contrast variation SANS investigation has proven that the status of the crystalline lattice
 can be monitored during the s-sPS sample treatment by observing the scattering features yielded at
 high angles. In Figure 5 we show the high Q scattering patterns from a dry s-sPS film. The film is

372 characterized by a high sulfonation degree ($S=46.3\%$) and a crystallinity of roughly 35%, and was
 373 clathrated with protonated toluene and subsequently loaded with C70 fullerenes. The data are
 374 presented two-dimensionally (Figure 5a) and averaged over the equatorial and meridian sectors
 375 (Figure 5b). The 010 reflections are well visible in the equatorial sectors, while the ionomer peak,
 376 which for the dry membrane is indicative of the mean distance between the sulfonic ionic clusters
 377 [44], shows an isotropic distribution. The inter-lamellar reflections appear at much lower Q values in
 378 the case of the sulfonated samples, and are thus not visible in this experimental configuration. This is
 379 due to the swelling of the inter-lamellar amorphous regions, as already reported in [23]. A
 380 correlation distance of $\xi_{\text{ion}}=2\pi/Q_{\text{ion}}=14.95 \text{ \AA}$ was obtained from the evaluation of the ionomer peak
 381 position in Q. This distance is smaller than the one determined for dry Nafion [45]. Taking into
 382 account the fact that the neutron SLD of fullerenes is very different from that of protonated toluene,
 383 but close to that of deuterated toluene [46], we may conclude that the replacement of the initial
 384 protonated toluene guest in the deuterated sPS crystalline region by the subsequently loaded
 385 fullerenes took place to a very small extent only, since the scattering features characteristic of the
 386 crystalline lattice were not affected apparently. Otherwise, the 010 reflections should have been
 387 reduced drastically, as in the case of using deuterated toluene as guest in the sPS co-crystals. Thus,
 388 the scattering features from the crystalline regions in the s-SPS films can be still observed after the
 389 loading of samples with fullerenes.

390



391

392

a)

b)

393 **Figure 5.** Two-dimensional SANS pattern from a dry s-SPS film containing the co-crystalline δ -phase
 394 with protonated toluene and loaded with C70 fullerenes (a) and one-dimensional scattering profiles
 395 from the same sample averaged over the equatorial (line) or meridian (symbol) directions,
 396 respectively (b). All data were collected at $L_D=2\text{m}$.

397

398 3.3. SANS on hydrated films – variation of hydration level.

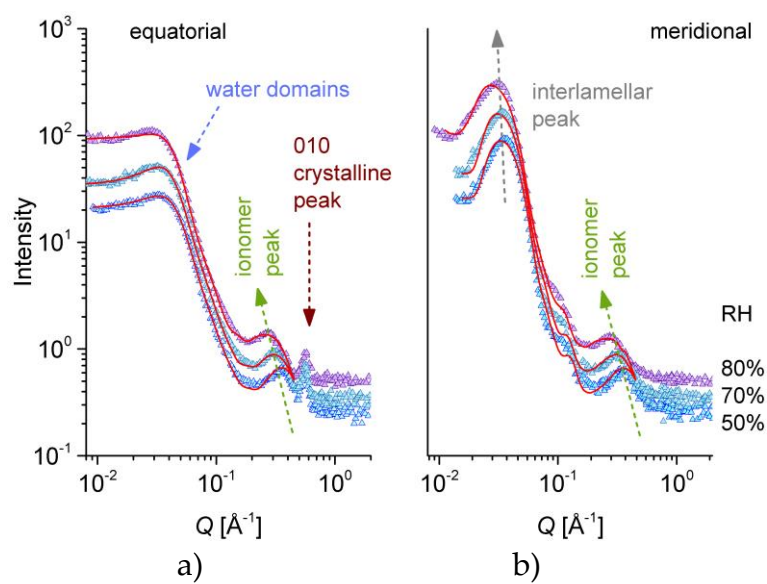
399

400 With this information at hand, two s-SPS samples with different degree of sulfonation and
 401 crystallinity, which were loaded with either C60 or C70, were investigated at the TOF SANS
 402 diffractometer TAIKAN during hydration at different RH levels and with different mixtures of
 403 $\text{H}_2\text{O}/\text{D}_2\text{O}$.

404 Figure 6 presents a selection of one-dimensional scattering data from the same s-SPS sample
 405 that was discussed in Figure 5, and which was hydrated with H_2O at different RH levels. The data
 406 were averaged over the meridian and the equatorial sectors. The scattering patterns present three
 407 distinct peak-like features, which are observable for all hydration levels. These features are
 408 indicative of structural levels occurring at different length scales in the complex morphology of the
 409 polymer films. In the high Q range, the 010 crystalline peak appears in the equatorial sectors at

410 around $Q_{010}=0.6 \text{ \AA}^{-1}$, as in the case of the sPS clathrates (Figure 4c) and the dry s-sPS sample (Figure 411 5b). This peak, which denotes a mean repeating distance between the sPS sheets of about 10-11 \AA , 412 does not change its position and intensity with the increase of the RH. This observation led to the 413 conclusion that the hydration does not affect the crystalline structure. Again, the neutron contrast is 414 provided by the protonated toluene guest molecules, which occupy the cavities between the 415 deuterated s-PS helices to a larger extent.

416 The ionomer peak is present in data on both the meridian and equatorial sectors, as it represents 417 a scattering feature characteristic of the hydration occurring in amorphous regions and is thus 418 isotropically distributed on the detection area. The peak position Q_{ion} depends on the level of the 419 film hydration [47, 48], thus it moves towards lower values of Q with increasing the RH. A detailed 420 presentation of the high Q scattering range from dry and hydrated films is given in Figure 7. In our 421 sample, the correlation between the hydrated ionic clusters increases from about $\xi_{\text{ion}}=14.95 \text{ \AA}$ for dry 422 film to about $\xi_{\text{ion}}=23.7 \text{ \AA}$ for hydrated film at RH=80%. A close inspection of the ionomer peak profile 423 reveals a shoulder like feature on the high Q side of the peaks, which becomes clearer with 424 increasing the humidity, due to the shift of the peak position to lower Q s. The Q -position of this 425 shoulder seems to remain constant regardless the RH and corresponds to the Q -position of the 426 ionomer peak characteristic of dry membrane. Apparently, a part of the ionic clusters giving rise the 427 occurrence of the ionomer peak in dry conditions are still not hydrated even for higher RH values. 428



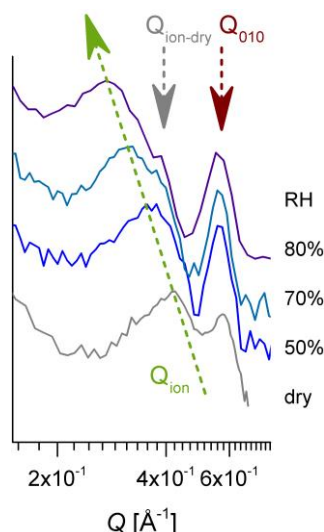
429
430

431 **Figure 6.** One-dimensional SANS patterns from the high sulfonated s-sPS film containing the 432 co-crystalline δ -phase with protonated toluene and loaded with C70 fullerenes hydrated at different 433 RH levels. Experimental data (symbols) averaged over the equatorial (a) or meridian (b) directions 434 are shown separately, with the lines corresponding to the model interpretation of the scattering 435 profiles, as discussed in text. The main structural features and their behavior with the variation of 436 RH are indicated.

437

438 In the low Q region the inter-lamellar peak characteristic of the oriented lamellar stacks (Figure 439 1) can be observed in the meridian scattering patterns. The peak position Q_{lam} moves only slightly to 440 lower Q values in increasing the RH, and denotes an inter-lamellar correlation of about 170-200 \AA . 441 On the other hand, the equatorial scattering patterns exhibit at low Q a kind of plateau and a 442 shoulder-like feature at around $Q=0.05 \text{ \AA}^{-1}$, which resemble characteristics of weakly correlated 443 spherical morphologies. We suppose that they represent loosely correlated large hydrated regions 444 that include the ionic clusters. The scattering from these water domains should appear isotropically 445 on the detector. However, in the meridian sectors the scattering from the lamellar stacks is 446 superimposing over it.

447 The scattering from these sulfonated s-sPS films characterized by a high sulfonation degree and
 448 a relatively high crystallinity, which are loaded with C70 fullerenes, resembles that from the
 449 fullerene free s-sPS films discussed in [23]. We may conclude that the partition of fullerenes between
 450 the amorphous and crystalline regions of these s-sPS films has a negligible effect on the scattering
 451 properties of the samples. As qualitatively concluded before, the C70 fullerenes seem to be located
 452 mostly in the amorphous regions rather than in the co-crystalline phase.
 453



454

455 **Figure 7.** The high-Q range of the SANS patterns on equatorial direction reported in Figure 6. The
 456 pattern from the membrane in dry state was added. The green arrow indicates the variation in the
 457 position of the ionomer peak in increasing the hydration, the dark red arrow marks the 010 reflection
 458 while the gray arrow points to the ionomer peak position characteristic of the membrane in dry state

459

460 On the other hand, the scattering from fullerenes dissolved in solution or amorphous polymer
 461 environment, like the deuterated polystyrene in the present case, is very weak [49], therefore we can
 462 consider it negligible compared to the contribution from other morphologies that are formed and
 463 evolve in our samples during sulfonation and hydration processes. The experimental results in
 464 Figure 6 were interpreted via structural models: the data on equatorial sectors were described by Eq.
 465 1-3 while the meridian patterns were described by a superposition of scattering from spherical
 466 domains and lamellar stacks (Eq. 4-6). The water domains were characterized by spherical form
 467 factor combined with the hard-sphere structure factor, an approach that is usually involved in
 468 interpretation of scattering data from spherical polymeric micelles [50, 51], but is applied also in the
 469 characterization of ionic aggregates in PEMs by scattering methods [52, 53]. Thus, four free
 470 parameters are used for describing the scattering from water domains in the Q range between 0.008
 471 and 0.2 Å⁻¹ according to Eq. 1-3, namely the “forward scattering” (I_0)^{sph} from the ensemble of the
 472 spherical water domains, the radius R of these domains, the hard sphere volume fraction η_{HS} and the
 473 hard-sphere radius R_{HS} . Additionally, we added a Gaussian term for the description of the ionomer
 474 peak at high Q and the constant background (Eq. 1). The three parameters of the Gaussian function
 475 describing the ionomer peak – amplitude, width and position – were left free during the fitting
 476 procedure, while the background was kept fixed, as given by the flat behavior of the scattering
 477 curves in the high Q range. The ionomer peak description was included in the model because of its
 478 presence in the meridian pattern too, which will help for an accurate modeling of these data in a
 479 subsequent step. The 010 peak was excluded from the fitting procedure. Despite the multitude of
 480 parameters, we consider that the fitting procedure offers reliable results, because the two structures
 481 that are modeled appear at very different length scales, therefore without influencing one another to
 482 a significant extent. On the other hand, if only the form factor is used for modeling the water
 483 domains, the experimental data cannot be properly described. The weak correlation effects between

484 the water domains seem to be a consequence of the high sulfonation degree of this sample, when
 485 water clusters are densely formed in the amorphous region. A detailed discussion about formation,
 486 growth and percolation of water clusters as a function of hydration level and functionalization of
 487 PEMs can be found in [9, 54].

488 Of a direct interest for the characterization of our system is the “forward scattering” from the
 489 ensemble of the spherical water domains and the size of these domains. We should note that a large
 490 polydispersity in size ($\sigma_R \approx 20\%$) of the water domains had to be considered in the fitting procedure in
 491 order to obtain a good fit in the Q region $0.1\text{--}0.2 \text{ \AA}^{-1}$. Knowing the size and the SLD of the scattering
 492 objects – the water domains, and the SLD of their environment – the sulfonated segments of s-SPS
 493 (Table 1), we could extract information about the volume fraction ϕ_{sph} occupied by the scattering
 494 objects in the sample (Eq. 1), in a similar way as reported in [55]. The volume fraction occupied by
 495 water in the whole amorphous region, $(\phi_{\text{water}})^{\text{amorphous}}$, is reported in Table 2. From the water volume
 496 fraction in the sample volume estimated from the interpretation of the $(I_0)^{\text{sph}}$, the reported value for
 497 each RH is obtained by taking into account the crystallinity of the film, which was estimated at 35%,
 498 and the fact that only the amorphous regions are hydrated.

499
 500 **Table 2.** The structural and scattering parameters of the hydrated and lamellar morphologies
 501 delivered by the model interpretation of the experimental data according to Eq. 1-7.

sample	condition	$R, \text{ \AA} / R_{\text{HS}}, \text{ \AA}$	$(\phi_{\text{water}})^{\text{amorphous}}, \%$	$\rho_{\text{lam}}, \times 10^{10} \text{ cm}^{-2}$	$L_b, \text{ \AA} / \sigma_D, \text{ \AA}$	$\rho_{\text{inter-lam}}, \times 10^{10} \text{ cm}^{-2}$	$(\phi_{\text{water}})^{\text{inter-lam}}, \%$
S=46.3%, with C70	RH=50% 100 H ₂ O / 0 D ₂ O	55.0 / 73.0	4.53	6.012	130.6 / 107.9	5.989	5.09
	RH=70% 100 H ₂ O / 0 D ₂ O	58.8 / 77.0	7.45	6.012	151.6 / 114.7	5.983	5.17
	RH=80% 100 H ₂ O / 0 D ₂ O	68.6 / 85.0	12.63	6.012	172.0 / 120.5	5.981	5.20
S=19.5%, with C60	RH=80% 100 H ₂ O / 0 D ₂ O	52 / -	18.20	6.003	159.2 / 99.3	5.989	5.10
	RH=80% 68 H ₂ O / 32 D ₂ O	52 / -	17.85	6.003	155.6 / 106.7	5.993	7.20
	RH=80% 0 H ₂ O / 100 D ₂ O	52 / -	18.50	6.003	135.4 / 110.9	5.999	-

502
 503 The data measured on the meridian sector were modeled for a morphology consisting of
 504 oriented crystalline-amorphous lamellar stacks, which are “embedded” in a bulk amorphous
 505 environment (Figure 1). The scattering was described by combining the Eq. 1 and 4-6 and was
 506 superimposed over the scattering from water domains (including the ionomer peak contribution),
 507 which is isotropic and is known from the model interpretation of the equatorial data. Assuming a
 508 very large lateral extension of the lamellae, $R_l > 1000 \text{ \AA}$, thus out of the size domain that is covered by
 509 the SANS window, and a constant thickness of the crystalline lamellae $d=60 \text{ \AA}$, an average value of
 510 what is reported in literature for sPS crystals with different degrees of crystallinity and subjected to
 511 different treatments [56], only two free size parameters were used in the fitting procedure, namely
 512 the thickness of the inter-lamellar layer, L_b , and the dispersion (smearing) parameter, σ_D , of the
 513 inter-lamellar spacing, $L_D=d+L_b$. As discussed in Section 2.3, the SLD of the crystalline and
 514 inter-lamellar amorphous layers, ρ_{lam} and $\rho_{\text{inter-lam}}$, were considered free during the fitting procedure
 515 while that of the bulk region ρ_{bulk} was considered that of the amorphous sPS (Table 1). Finally, the
 516 volume fraction of lamellar stacks in Eq. 1 was considered fixed and taken from the assumed
 517 crystalline degree of the material (35%).

518 All three experimental curves in Figure 6b were modeled simultaneously. Since the crystalline
519 lamellae are not changing during hydration, the ρ_{lam} free parameter was considered the same for all
520 curves while the other free parameters were left to vary specifically to each RH condition. The model
521 lines in Figure 6b are describing rather well the experimental data and the fitting procedure
522 delivered the main parameters reported in Table 2. As we already noted, the sulfonation of the
523 amorphous regions in the sPS film induced a swelling of the inter-lamellar domains in comparison
524 with the non-sulfonated films, as reported in [23], so slightly larger value for the thickness of the
525 inter-lamellar layer L_b , hence the inter-lamellar spacing L_D , as reported in the literature for the sPS
526 crystals was obtained in our case. This quantitative analysis indicates a certain swelling of the
527 inter-lamellar regions with increasing hydration, deduced from the slight increase in the thickness of
528 the inter-lamellar layer L_b . However, we should note that the model interpretation of the current
529 data indicates also an increase in the smearing σ_D of the fitted inter-lamellar correlation distance
530 between the oriented lamellae $L_D=d+L_b$, which makes the actual swelling of the amorphous
531 inter-lamellar layer difficult to assess.

532 To obtain semi-quantitative information about the volume fraction of water accumulated in the
533 inter-lamellar amorphous region, the fitted SLD was further interpreted based on the assumptions
534 made on the polymer and water volume fractions in these regions (Section 2.3). Thus, at low
535 hydration level the water fraction in the inter-lamellar space is rather similar to that in the whole
536 amorphous regions of the film sample. With increasing RH the water domains grow in size and
537 number apparently (Table 2). From the evaluated values for $(\phi_{\text{water}})_{\text{amorphous}}$ and $(\phi_{\text{water}})_{\text{inter-lam}}$ we can
538 conclude that the formation and growth of the water domains with increasing hydration seem to
539 happen almost only in the amorphous bulk region while the water volume fraction in the
540 inter-lamellar amorphous layers remains quite constant. This may explain also the aspect of the
541 ionomer peak (Figure 7), due to ionic clusters that are remaining dry still at high RH values. Also,
542 keeping in mind that the hydrated regions are characterized by a large polydispersity in size, we can
543 assume that smaller water domains are present in the inter-lamellar regions compared to the bulk
544 regions. These effects may be caused by the increased flexibility of the sPS chains in the bulk
545 amorphous domains compared to that of the amorphous sPS chains between the crystalline
546 lamellae, which favors the formation and growth of water domains mostly in the bulk amorphous
547 region. For very high hydration levels, RH>85%, a growth and percolation of water domains takes
548 place in the bulk region, which ultimately leads to changes in the orientation and position of lamellar
549 stacks, as reported before [23]. The preservation of the lamellar stacks arrangements even at very
550 high hydration level (saturation) is indicative of the lower water uptake in the inter-lamellar
551 amorphous regions as in the bulk amorphous ones.

552 Finally, the fitting procedure delivered the value $\rho_{\text{lam}}=6.012 \times 10^{10} \text{ cm}^{-2}$ for the SLD of the
553 crystalline lamellae, a value which is lower than that of crystalline sPS (Table 1). If we consider that
554 the sPS lamellae are loaded with protonated toluene guest, from the interpretation of the fitted value
555 we obtain a volume fraction of about 8.2% protonated toluene hosted between the sPS helices in the
556 crystalline region, a value in very good agreement with what is reported in literature [25].
557

558 3.4. SANS on hydrated films – neutron contrast variation.

559
560 The equatorial and meridional scattering patterns from the s-sPS film with a low degree of
561 sulfonation ($S=19.3\%$) and lower crystallinity (22%), which was loaded with C60 fullerenes, are
562 presented in Figure 8 as they were collected at a constant hydration level, RH=80%, which was
563 achieved by using different $\text{H}_2\text{O}/\text{D}_2\text{O}$ mixtures. Three neutron contrast conditions corresponding to
564 the $\text{H}_2\text{O}/\text{D}_2\text{O}$ ratios (vol%) of 100/0, 68/32 and 0/100 were investigated. The middle ratio corresponds
565 to the matching of the calculated SLD for the sulfonic acid terminal group (SO_3H).

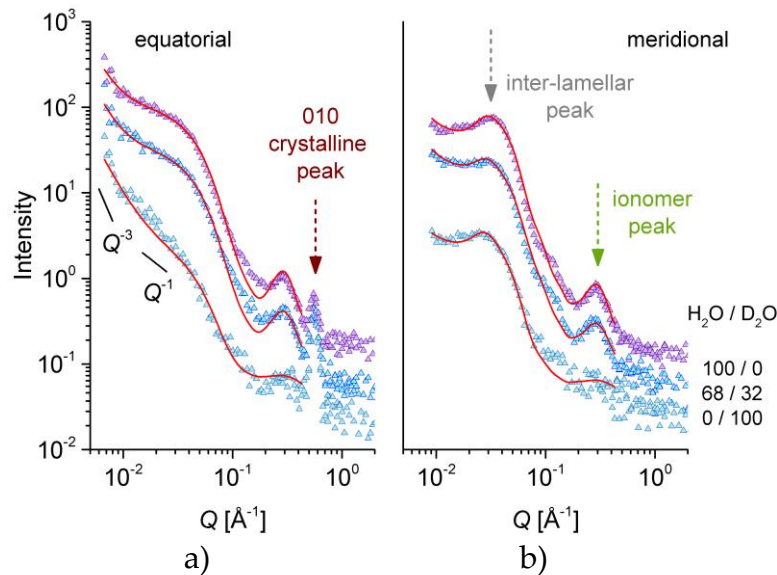
566 For the 100/0 $\text{H}_2\text{O}/\text{D}_2\text{O}$ case, the same scattering features as in the case of the sample with a high
567 degree of sulfonation (Figure 6) can be observed: the 010 crystalline peak that is revealed only in the
568 equator direction, the isotropic ionomer peak that is visible in both the equatorial and meridian

569 scattering patterns and the inter-lamellar peak that is observed only in the meridian direction, at a
570 lower Q value than the ionomer peak. The profile of the inter-lamellar correlation peak is not as
571 strong as in the case of the sample with higher sulfonation degree (Figure 6), which may be due to
572 the lower crystallinity in the present sample. Unlike for the high sulfonation degree sample, in the
573 present case the scattering from the water domains (equatorial sectors) does not show a shoulder
574 like feature at around $Q=0.05 \text{ \AA}^{-1}$. Instead, a strong upturn appears towards lower Qs. A similar
575 feature was observed in the very low Q region of the scattering patterns from highly sulfonated films
576 [23]. The absence of the shoulder like feature indicates that there is no correlation effect between the
577 water domains. This may be due to the lower sulfonation degree in the present sample, which makes
578 the water domains to form and grow in the amorphous regions well separated from each other. On
579 the other hand, the upturn at low Q, which appears stronger on the equator direction due to
580 stretching of sample on vertical axis, arises from the large-scale fractal-like character of the
581 membranes. This feature is not visible towards low Q in the patterns reported in Figure 6. This may
582 be a consequence of the stronger correlation effects between the lamellae in the stack in that case: the
583 strong structure factor peak induces an intensity drop towards low Q and consequently the intensity
584 upturn is becoming observable at lower Q values. The intensity upturn at low Q can be described by
585 a power law [23, 31], which should be added to the model equations that are used for fitting the
586 experimental data, but is less important for the data interpretation in this work. The 70/30 H₂O/D₂O
587 data show basically the same scattering features that are shown by the 100/0 H₂O/D₂O patterns, only
588 the global intensity is lower, due to lower contrast achieved between hydrated and non-hydrated
589 components of the film morphology. No matching of any scattering feature is visible. The data
590 measured under the 0/100 H₂O/D₂O contrast show a different behavior from the other two contrast
591 conditions. The first striking effect is the vanishing of the ionomer peak. We assume that the
592 matching of the scattering properties of ionic clusters and surrounding water is achieved, which
593 renders the correlation between the ionic clusters not anymore visible. From this observation, a very
594 important conclusion may be drawn: the ionic clusters that are promoting the water uptake by the
595 membrane consist of an association of larger sections of neighboring s-sPS chains in the region of the
596 benzene ring and the sulfonic acid terminal group, which are correlated over the distance $2\pi/Q_{\text{ion}}$.
597 With increasing hydration, the water domain grows and the correlation distance between these
598 groups increases. The correlation effects are vanishing in the scattering patterns when the hydration
599 medium has a similar SLD to that of the sulfonated sPS segment, which is roughly the D₂O case.

600 Another peculiarity of the scattering data in this contrast condition is the low Q behavior, where
601 a Q^{-1} power law behavior of the scattered intensity may be roughly identified in the equatorial
602 profile, rather than the spherical form factor profile combined with a low-Q steeper power law
603 feature, as for the other contrast conditions or the case of the highly sulfonated sample [23]. The Q^{-1}
604 power law behavior is indicative of one-dimensional structures present in the sample. If we consider
605 that the water accumulates along groups of elongated s-sPS chains in the amorphous region, this
606 will highlight the hydrated regions as one-dimensional arrangements in contrast to the surrounding
607 crystalline or non-sulfonated sPS environment, which is in agreement with the observed scattering
608 behavior.

609 The interpretation of the experimental data was done in a similar way as for the sPS film with
610 higher sulfonation degree (Figure 6). The equatorial data were described by the combination of a
611 spherical form factor of the water clusters (Eq. 2) and a Gaussian feature of the ionomer peak. An
612 additional Q^{-3} power-law term was added to describe the low-Q data behavior. The meridian data
613 were fitted by a superposition of the scattering features from the water clusters and the correlated
614 lamellar stacks (Eq. 4-6). The modeling of the experimental data was quite successful and has
615 delivered the parameters reported in Table 2. For the description of the equatorial data only a
616 spherical form factor was considered, as no tracks of correlation between the water clusters was
617 observed. The experimental data were separately fitted on the equatorial sectors first, to obtain the
618 water domains parameters, and then on the meridian direction, simultaneously for all contrast
619 conditions. The fitting procedure was carried out as discussed in the Section 3.3. The L_b parameter
620 was fitted, but kept the same for all contrast condition, since they were measured at the same RH.

621 The low-Q power law behavior was considered only for the equatorial data interpretation, where it
 622 is more prominent due to the uni-axial sample deformation on vertical direction.
 623



624
 625 a) b)

626 **Figure 8.** One-dimensional SANS patterns from the low sulfonated s-SPS film containing the
 627 co-crystalline δ -phase with protonated toluene and loaded with C60 fullerenes hydrated at RH=80%
 628 with different H₂O/D₂O ratios, as indicated in the right side of the plots. Experimental data
 629 (symbols) averaged over the equatorial (a) or meridian (b) directions are shown separately, with the
 630 lines corresponding to the model interpretation of the scattering profiles, as discussed in text. The
 631 main structural features are indicated by arrows while the solid lines in the panel a) indicate the
 632 power law behavior of the scattering intensity in different Q ranges.

633
 634 The volume fraction that is occupied by water in the whole sample is roughly the same for all
 635 contrast conditions, about 18%, which is a normal behavior, since all measurements were carried out
 636 at the same RH. From the fitted SLD of the inter-lamellar layers, semi-quantitative information about
 637 the volume fraction occupied by water in these regions could be obtained. Thus, the water occupies
 638 between 5% and 7%, as delivered by the fit of the 100/0 and 70/30 contrast conditions. The fitted
 639 results for the 0/100 contrast condition could not be further interpreted in a reliable way. A value
 640 with no physical meaning was obtained therefore we believe that in this case a more specific model
 641 should be used for the interpretation of the experimental data. Anyway, all values obtained for the
 642 lamellar stacks in the other two contrast conditions are consistent with each other. This makes the
 643 model interpretation of these data to be considered realistic. Finally, the value $\rho_{lam}=6.003 \times 10^{10} \text{ cm}^{-2}$
 644 for the SLD of the crystalline lamellae delivered a volume fraction of about 8.5% protonated toluene
 645 hosted between the sPS helices in the crystalline region, again a value in very good agreement with
 646 what is reported in literature [25].
 647

648 4. Conclusions

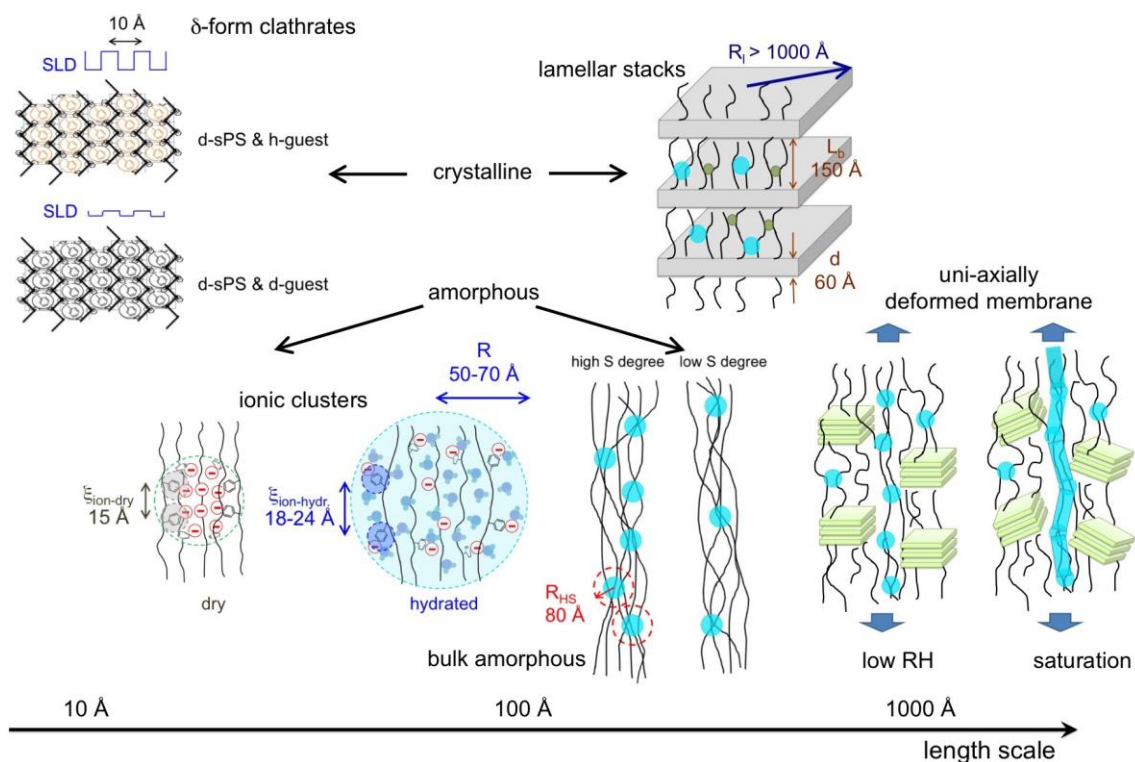
649 SANS with contrast variation was used to resolve the complex morphology of the sulfonated
 650 semi-crystalline syndiotactic polystyrene membranes at different hydration levels. Samples with
 651 different crystalline degree and loaded with different guest molecules in either the crystalline or the
 652 amorphous regions were studied for different sulfonation degrees achieved by using the solid-state
 653 sulfonation procedure, which only affects the amorphous regions and leaves the crystallinity
 654 unchanged. The exchange between deuterated and protonated toluene in the cavities between the
 655 SPS helices of the crystalline δ -form allowed for the variation of the neutron SLD of crystalline
 656 lamellae. The loading of membranes with fullerenes, which improve resistance to oxidation

657 decomposition, seems to affect to a greater extent the amorphous phase of the films rather than the
 658 crystalline one. The use of uni-axially deformed films allowed the separation on different detection
 659 sectors of the scattering from structures of similar size but different orientation and functionality,
 660 which compose the dry and hydrated membrane morphologies. On the other hand, the investigation
 661 carried out over a wide Q-range allowed the observation and characterization with models of
 662 structures that appear and evolve with increasing humidity at different length scales.

663 According to our qualitative and quantitative analysis, the hydration water is distributed to the
 664 same extent in the inter-lamellar and bulk amorphous regions at low hydrations, whereas with
 665 increasing the hydration level the water accumulates predominantly in the bulk amorphous region.
 666 The contrast variation measurements revealed that the ionic clusters that are promoting the
 667 hydration and conductivity of the membranes consist not only of sulfonic groups but also segments
 668 of sPS that are affected by sulfonation process. At very high hydration levels (saturation), the water
 669 domains evolve in water channels, which induce a displacement and change in orientation of
 670 lamellar stacks [23]. Nevertheless, the crystallinity, hence the robustness of membrane, is preserved.

671 A global picture of the multiple structural level character of the membrane morphology, as
 672 resulted from the SANS analysis, is reported in Figure 9.

673



674

675 **Figure 9.** Structural levels that form on the length scale between nm and μm in dry and hydrated
 676 membranes based on semi-crystalline s-sPS, as identified and characterized by contrast variation
 677 SANS. The turquoise full circles distributed in the bulk and inter-lamellar amorphous regions
 678 represent the hydrated ionic clusters while the green small dots in the inter-lamellar amorphous
 679 layers are the still dry ionic clusters. At very high hydration levels (saturation) water channels are
 680 formed in the bulk amorphous regions [23].

681

682 **Acknowledgments:** The help from Dr. Oreste Tarallo (Universita' degli Studi di Napoli Federico II, Italy), Dr.
 683 Rocco di Girolamo (Universita' degli Studi di Napoli Federico II, Italy) and Dr. Lucia Caporaso (Universita'
 684 degli Studi di Salerno, Italy) on synthesis of the deuterated syndiotactic polystyrene is gratefully
 685 acknowledged. We are very thankful to Dr. Zsolt Revay for help with the neutron prompt gamma activation
 686 measurements and to Eng. Toshiaki Morikawa for his support during the experiment at TAIKAN SANS

687 diffractometer. The neutron experiment at the Materials and Life Science Experimental Facility of the J-PARC
688 was performed under a user program (Proposal No. 2017B0183, BL15 TAIKAN).

689

690 **Conflicts of Interest:** "The authors declare no conflict of interest."

691 **References**

- 692 1. Eberle, U; Mueller, B; v.Helmolt, R. Fuel Cell Electric Vehicles and Hydrogen Infrastructure: Status 2012. *Energy Environ. Sci.* **2012**, *5*, 8780-8797.
- 693 2. Barbir, F. Fuel Cells Applications. In *PEM Fuel Cells*, 2nd ed.; Barbir, F., Ed.; Elsevier Inc. 2013, pp. 373-434.
- 694 3. Kravtsberg, A.; Ein-Eli, Y. Review of Advanced Materials for Proton Exchange Membrane Fuel Cells. *Energy Fuels* **2014**, *28*, 7303-7330.
- 695 4. Hayashi, A.; Nishihara, M.; Matsuda, J.; Sasaki, K. Polymer electrolyte Fuel Cells (PEFCs). In *Hydrogen Energy Engineering. Green Energy and Technology*, Sasaki, K.; Li, H.-W.; Hayashi, A.; Yamabe, J.; Ogura, T.; Lyth, S.M., Eds.; Springer, Tokyo, 2016, pp. 301-311.
- 696 5. Kreuer, K.-D.; Paddison, S.J.; Spohr, E.; Schuster, M. Transport in Proton Conductors for Fuel-Cell Applications: Simulations, Elementary Reactions, and Phenomenology. *Chem. Rev.* **2004**, *104*, 4637-4678.
- 697 6. Okada, T. Theory for Water Management in Membranes for Polymer Electrolyte Fuel Cells - Part 1 The Effect of Impurity Ions at the Anode Side on the Membrane Performance. *J. Electroanal. Chem.* **1999**, *465*, 1-17.
- 698 7. St.Pierre, J.; Wilkinson, D.P.; Knights, S.; Bos, M.L. Relationships Between Water Management, Contamination and Lifetime Degradation in PEFC. *J. New Mater. Electrochem. Syst.* **2000**, *3*, 99-106.
- 699 8. Huguet, P.; Morin, A.; Gebel, G.; Deabate, S.; Sutor, A.K.; Peng, Z. In Situ Analysis of Water Management in Operating Fuell Cells by Confocal Raman Spectroscopy. *Electrochem. Commun.* **2011**, *13*, 418-422.
- 700 9. Kusoglu, A.; Weber, A.Z. New Insights into Perfluorinated Sulfonic-Acid Ionomers. *Chem. Rev.* **2017**, *117*, 987-1104.
- 701 10. Smitha, B.; Sridhar, A.; Khan, A.A. Solid Polymer Electrolyte Membranes for Fuel Cell Applications—a Review. *J. Membrane Sci.* **2005**, *259*, 10-26.
- 702 11. Hickner, M.A.; Ghassemi, H.; Kim, Y.S.; Einsla, B.R.; McGrath, J.E. Alternative Polymer System for Proton Exchange Membranes (PEMs). *Chem. Rev.* **2004**, *104*, 4587-4612.
- 703 12. Hihashihara, T.; Matsumoto, K.; Ueda, M. Sulfonated Aromatic Hydrocarbon Polymers as Proton Exchange Membranes for Fuel Cells. *Polymer* **2009**, *50*, 5341-5357.
- 704 13. Zhang, Y.; Li, J.; Ma, L.; Cai, W.; Cheng, H. Recent Developments on Alternative Proton Exchange Membranes: Strategies for Systematic Performance Improvement. *Energy Technol.* **2015**, *3*, 675-691.
- 705 14. Zhao, Y.; Yoshida, M.; Oshima, T.; Koizumi, S.; Rikukawa, M.; Szekely, N.; Radulescu, A.; Richter, D. Elucidation of the Morphology of the Hydrocarbon Multiblock Copolymer Electrolyte Membranes for Proton Exchange Fuel Cells. *Polymer* **2016**, *86*, 157-167.
- 706 15. Feng, S.; Kondo, S.; Kaseyama, T.; Nakazawa, T.; Kikuchi, T.; Selyanchyn, R.; Fujikawa, S.; Christiani, L.; Sasaki, K.; Nishihara, M. Development of Polymer-Polymer Type Charge-Transfer Blend Membranes for Fuel Cell Application. *J. Membrane Sci.* **2018**, *548*, 223-231.
- 707 16. Boriello, A.; Agoretti, P.; Ambrosio, L.; Fasano, G.; Pellegrino, M.; Venditto, V.; Guerra, G. Syndiotactic Polystyrene Films with Sulfonated Amorphous Phase and Nanoporous Crystalline Phase. *Chem. Mater.* **2009**, *21*, 3191-3196.
- 708 17. Saga, S.; Matsumoto, H.; Saito, K.; Minagawa, M.; Tanioka, A. Polyelectrolyte Membranes Based on Hydrocarbon Polymer Containing Fullerenes. *J. Power Sources* **2008**, *176*, 16-22.
- 709 18. Fasano, G.; Califano, R.; Pellegrino, M.; Venditto, V.; Guerra, G.; Boriello, A.; Ambrosio, L.; Sansone, L. Semicrystalline proton-conductive membranes with sulfonated amorphous phases. *Int. J. Hydrol. Energy* **2011**, *36*, 8038-8044.
- 710 19. Jaymand, M. Recent Progress in the Chemical Modification of Syndiotactic Polystyrene. *Polym. Chem.* **2014**, *5*, 2663-2690.
- 711 20. Tashiro, K.; Ueno, I.; Yoshioka, A.; Kobayashi, M. Molecular Mechanism of Solvent-Induced Crystallization of Syndiotactic Polystyrene Glass. 1. Time-Resolved Measurements of Infrared/Raman Spectra and X-Ray Diffraction. *Macromolecules* **2001**, *34*, 310-315.

738 21. Raut, P.; Liang, W.; Chen, Y-M.; Zhu, Y.; Jana, S.C. Syndiotactic Polystyrene-Based Ionogel Membranes for
739 High Temperature Electrochemical Applications. *ACS Appl. Mater. Interfaces* **2017**, *9*, 30933-30942.

740 22. Kreuer, K-D.; Portale, G. A Critical Revision of the Nano-Morphology of Proton Conducting Ionomers and
741 Polyelectrolytes for Fuel Cell Applications. *Adv. Funct. Mater.* **2013**, *23*, 5390-5397.

742 23. Schiavone, M-M.; Tarallo, O.; Di Girolamo, R.; Caporaso, L.; Appavou, M-S.; Revay, Z.; Radulescu, A.
743 Structure and Morphology of Model Polymer electrolyte Membranes based on Sulfonated
744 Syndiotactic-Polystyrene in the δ Co-crystalline Phase Resolved by Small-Angle Neutron Scattering. *Solid
745 State Ionics* **2018**, *320*, 392-406.

746 24. De Rosa, C.; Guerra, G.; Petraccone, V.; Pirozzi, B. Crystal Structure of the Emptied Clathrate Form (δ
747 Form) of Syndiotactic Polystyrene. *Macromolecules* **1997**, *30*, 4147-4152.

748 25. Albunia, A.R.; d'Aniello, C.; Guerra, G. Three Different Co-crystalline Phases of Syndiotactic Polystyrene
749 with a Nitroxide Radical. *Cryst. Eng. Comm.* **2010**, *12*, 3942-3949.

750 26. Kaneko, F.; Radulescu, A.; Ute, K. Time-resolved SANS Studies on Guest Exchange Processes in
751 Co-Crystals of Syndiotactic Polytyrene. *Polymer* **2013**, *54*, 3145-3149.

752 27. Radulescu, A.; Szekely, N.K.; Appavou, M-S.; Pipich, V.; Kohnke, T.; Ossovyi, V.; Staringer, S.; Schneider,
753 G.J.; Amann, M.; Zhang-Haagen, B.; Brandl, G.; Drochner, M.; Engels, R.; Hanslik, R.; Kemmerling, G.
754 Studying Soft-Matter and Biological Systems over a Wide Length-Scale from Nanometer and Micrometer
755 Sizes at the Small-Angle Neutron Diffractometer KWS-2. *J. Vis. Exp.* **2016**, e54639.

756 28. DeCaluwe, S.C.; Kienzle, P.A.; Bhargava, P.; Baker, A.M.; Dura, J.A. Phase Segregation of Sulfonate
757 Groups in Nafion interface Lamellae, Quantified via Neutron Reflectometry Fitting Techniques for
758 Multi-layered Structures. *Soft Matter* **2014**, *10*, 5763-5776.

759 29. Takata, S.; Suzuki, J.; Shinohara, T.; Oku, T.; Tominaga, T.; Ohishi, K.; Iwase, H.; Nakatani, T.; Inamura, Y.;
760 Ito, T.; Suzuya, K.; Aizawa, K.; Arai, M.; Otomo, T.; Sugiyama, M. The design and Q Resolution of the
761 Small and Wide Angle Neutron Scattering Instrument (TAIKAN) in J-Parc. *JPS Conf. Proc.* **2015**, *8*, 036020.

762 30. Pedersen, J.S. Determination of Size Distribution from Small-Angle Scattering Data for Systems with
763 Effective Hard-Sphere Interactions. *J. Appl. Cryst.* **1994**, *27*, 595-608.

764 31. Radulescu, A.; Fetters, L.J.; Richter, D. Polymer-Driven Wax Crystal Control Using Partially Crystalline
765 Polymeric Materials. *Adv. Pol. Sci.* **2008**, *210*, 1-100.

766 32. Asano, A. Free Volume Study of Amorphous Polymers Detected by Solid-State ^{13}C -NMR Linewidth
767 Experiments. *J. Chem. Phys.* **2001**, *115*, 8665-8669.

768 33. Revay, Z. Determining Elemental Composition Using Prompt γ Activation Analysis. *Anal. Chem.* **2009**, *81*,
769 6851-6859.

770 34. Weiss, R.A.; Sen, A.; Willis, C.L.; Pottick, L.A. Block Copolymer Ionomers: 1. Synthesis and Physical
771 Properties of Sulphonated Poly(Styrene-Ethylene/Butylene-Styrene). *Polymer* **1991**, *32*, 1867-1874.

772 35. Sheng, L.; Higashihara, T.; Nakazawa, S.; Ueda, M. Polystyrenes Containing Flexible Alkysulfonated Side
773 Chains as a Proton Exchange Membrane for Fuel Cell Applications. *Polym. Chem.* **2012**, *3*, 3289-3295.

774 36. Huang, T.; Jin, B.; Peng, R.F.; Chen, C.D.; Zheng, R.Z.; He, Y.; Chu, S.J. Synthesis and Characterization of
775 [60]Fullerenes-Glycidyl Azide Polymer and Its Thermal Decomposition. *Polymers* **2015**, *7*, 896-908.

776 37. Wang, C.; Ruan, L.; Chang, X-L.; Zhang, X.; Yang, S-T.; Guo, X.; Yuan, H.; Guo, C.; Shi, W.; Sun, B.; Zhao,
777 Y. The Isotopic Effect of ^{13}C -Labeled Large Carbon Cage (C_{70}) Fullerenes and Their Formation Process. *RSC
778 Adv.* **2015**, *5*, 76949-76956.

779 38. Wu, Z.C.; Jelski, D.A.; George, T.F. Vibrational motions of Buckminsterfullerenes. *Chem. Phys. Letters* **1987**,
780 137, 291-294.

781 39. Kobayashi, M.; Yoshioka, T.; Imai, M.; Itoh, Y. Structural Ordering on Physical Gelation of Syndiotactic
782 Polystyrene Dispersed in Chloroform Studied by Time-Resolved Measurements of Small Angle Neutron
783 Scattering (SANS) and Infrared Spectroscopy. *Macromolecules* **1995**, *28*, 7376-7385.

784 40. Bogdanov, A.A.; Voznyakovskii, A.P.; Pozdnya, A.O. UV-Vis Diagnostics of the PMMA- C_{60} Composite
785 System and the Kinetics of its Thermal Decomposition. *Nanosystems: physics, chemistry, mathematics* **2014**, *5*,
786 62-66.

787 41. Scharff, P.; Risch, K.; Carta-Abelmann, L.; Dmytruk, I.M.; Bilyi, M.M.; Golub, O.A.; Khavryuchenko, A.V.;
788 Buzaneva, E.V.; Aksenov, V.L.; Avdeev, M.V.; Prylutskyy, Yu.I.; Durov, S.S. Structure of C_{60} Fullerene in
789 Water: Spectroscopic Data. *Carbon* **2004**, *42*, 1203-1206.

790 42. Chakraborty, C.; Malik, S.; Guenet, J-M. Syndiotactic Polystyrene / Fullerene Composites: Elucidation of
791 Structural Aspect. *Macromol. Symp.* **2011**, *303*, 56-62.

792 43. Kaneko, F.; Radulescu, A.; Ute, K. Time-Resolved Small-Angle Neutron Scattering Study on
793 Guest-Exchange Processes in Co-Crystals of Syndiotactic Polystyrene. *J. Appl. Cryst.* **2014**, *47*, 6-13.

794 44. Zhao, Y.; Yoshida, M.; Oshima, T.; Koizumi, S.; Rikukawa, M.; Szekely, N.; Radulescu, A.; Richter, D.
795 Elucidation of the Morphology of the Hydrocarbon Multi-Block Copolymer Electrolyte Membranes for
796 Proton Exchange Fuel Cells. *Polymer* **2016**, *86*, 157-167.

797 45. Gebel, G. Structural evolution of water swollen perfluorosulfonated ionomers from dry membrane to
798 solution. *Polymer* **2000**, *41*, 5829-5838.

799 46. R. Dattani, R. Michels, A.J. Nedoma, R. Schweins, P. Westacott, K. Huber, J.T. Cabral, *Macromolecules* **47**,
800 6113-6120, 2014

801 47. Fumagalli, M.; Lyonnard, S.; Prajapati, G.; Berrod, Q.; Porcar, L.; Guillermo, A.; Gebel, G. Fast Water
802 Diffusion and Long-Term Polymer Reorganization during Nafion Membrane Hydration Evidenced by
803 Time-Resolved Small-Angle Neutron Scattering. *J. Phys. Chem. B* **2015**, *119*, 7068-7076.

804 48. Lyonnard, S. Structure and Transport Properties of Polymer Electrolyte Membranes Probed at
805 Microscopic Scales. In *Alternative energies, Advanced Structured Materials*; G. Ferreira, Ed.; Springer-Verlag
806 Berlin Heidelberg, 2013; Volume 34; pp. 163-193.

807 49. Melnichenko, Y.B.; Wignall, G.D.; Compton, R.N.; Bakale, G. Characterization of Fullerenes and Fullerene
808 Derivatives by Small-Angle Neutron Scattering and Transmission Measurements. *J. Chem. Phys.* **1999**, *111*,
809 4724-4728.

810 50. He, L.; Garamus, V.M.; Funari, S.S.; Malfois, M.; Willumeit, R.; Niemeyer, B. Comparison of Small-Angle
811 Scattering Methods for the Structural Analysis of Octyl- β -Maltopyranoside Micelles. *Macromolecules* **2002**,
812 106, 7596-7604.

813 51. Stellbrink, J.; Rother, G.; Laurati, M.; Lund, R.; Willner, L.; Richter, D.
814 Poly(ethylene-alt-propylene)-Poly(ethylene oxide) Diblock Copolymer Micelles: A Colloidal Model
815 System with Tunable Softness. *J. Phys.: Condens. Matter* **2004**, *16*, S3821-S3834.

816 52. Gebel, G.; Moore, B. Small-Angle Scattering Study of Short Pendant Chain Perfluorosulfonated Ionomer
817 Membranes. *Macromolecules* **2000**, *33*, 4850-4855.

818 53. Gebel, G., Structure of Membranes for Fuel Cells: SANS and SAXS Analyses of Sulfonated PEEK
819 Membranes and Solutions. *Macromolecules* **2013**, *46*, 6057-6066.

820 54. Kusoglu, A.; Ionomer Thin Films in PEM Fuel Cells. In *Encyclopedia of Sustainability Science and Technology*;
821 Meyers, R.A., Ed.; Springer New York NY, USA, 2018; pp. 1-23.

822 55. Radulescu, A.; Schwahn, D.; Monkenbusch, M.; Fetters, L.J.; Richter, D. Structural Study of the Influence of
823 Partially Crystalline Poly(ethylene butene) Random Copolymers on Paraffin Crystallization in Dilute
824 Solutions. *J. Pol. Sci. B, Pol. Phys.* **2004**, *42*, 3113-3132.

825 56. Wang, H.; Wu, C.; Wui, D.; Men, Y. Lamellar Thickness Dependence of Crystal Modification Selection in
826 the Syndiotactic Polystyrene γ -to- α/β Phase Transition Process. *Macromolecules* **2018**, *51*, 497-503.